Viscous hydrodynamic evolution of neutron star merger accretion disks: A code comparison

Rodrigo Fernández,[1,*] Oliver Just,[2,3] Zewei Xiong,[2] and Gabriel Martínez-Pinedo[2,4]

[1]*Department of Physics, University of Alberta, Edmonton, Alberta T6G 2E1, Canada*
[2]*GSI Helmholtzzentrum für Schwerionenforschung, Planckstraße 1, D-64291 Darmstadt, Germany*
[3]*Astrophysical Big Bang Laboratory, RIKEN Cluster for Pioneering Research, 2-1 Hirosawa, Wako, Saitama 351-0198, Japan*
[4]*Institut für Kernphysik (Theoriezentrum), Fachbereich Physik, Technische Universität Darmstadt, Schlossgartenstraße 2, D-64289 Darmstadt, Germany*

(Received 29 June 2023; accepted 21 May 2024; published 1 July 2024)

The accretion disk formed after a neutron star merger is an important contributor to the total ejecta from the merger, and hence to the kilonova and the *r*-process yields of each event. Axisymmetric viscous hydrodynamic simulations of these disks can capture thermal mass ejection due to neutrino absorption and in the advective phase—after neutrino cooling has subsided—and are thus likely to provide a lower limit to the total disk ejecta relative to magnetohydrodynamic evolution. Here we present a comparison between two viscous hydrodynamic codes that have been used extensively on this problem over the past decade; ALCAR and FLASH. We choose a representative setup with a black hole at the center, and vary the treatment of viscosity and neutrino transport. We find good overall agreement ($\sim$10% level) in most quantities. The average outflow velocity is sensitive to the treatment of the nuclear binding energy of heavy nuclei, showing a larger variation than other quantities. We postprocess trajectories from both codes with the same nuclear network, and explore the effects of code differences on nucleosynthesis yields, heating rates, and kilonova light curves. For the latter, we also assess the effect of varying the number of tracer particles in reconstructing the spatial abundance distribution for kilonova light curve production.

DOI: 10.1103/PhysRevD.110.023001

I. INTRODUCTION

Production of chemical elements heavier than iron in the Universe via the rapid neutron capture process (*r*-process) has thus far been established observationally for neutron star (NS) mergers through the kilonova associated with GW170817 (e.g., [1,2]). The accretion disk formed during the merger is a significant or even dominant contributor to the ejecta—depending on binary parameters—launching outflows on timescales ranging from a few ms to several seconds after the merger (e.g., [3–6]).

Multiple processes can lead to mass ejection from the disk; dissipation of magnetorotational turbulence, nuclear recombination, neutrino absorption, and magnetic stresses if a large-scale magnetic field is present at disk formation or generated via dynamo action (e.g., [7,8]). Neutrino cooling is important in all disks with initial masses $\gtrsim 10^{-3} M_\odot$ (e.g., [9–13]), but it subsides on a timescale of several $\sim$100 ms in disks around black holes (BHs) due to the drop in temperature and density associated with accretion. The absence of cooling leads to ejection driven by viscous heating and nuclear recombination [14]. When a NS is present, energy deposition by neutrino absorption can also make a significant contribution to driving the outflow (e.g., [15–18]).

The magnetic field strength and geometry at disk formation determines the importance of prompt mass ejection due to magnetic stresses and the possible emergence of a jet (e.g., [19]). These magnetic properties are currently an active area of research. For BH central objects, the only *ab initio* study thus far [20,21] indicates that large scale field formation is not ubiquitous, with the corresponding absence of prompt ($\sim$ms) mass ejection via magnetic stresses. Thus, in the case of BH central objects, thermal mass ejection due to the drop in neutrino cooling is the only outflow channel established as robust thus far.

Long-term viscous hydrodynamic models of the disk outflow have been carried out for a decade now, and have led to most of our current understanding of the disk ejecta [8,15–17,22–33]. For BH remnants, these simulations are able to capture thermal mass ejection to good approximation, as demonstrated by detailed comparison with general

*rafernan@ualberta.ca

relativistic magnetohydrodynamical (GRMHD) simulations [34]. Viscous hydrodynamic simulations thus provide a good estimate for the lower limit to the mass ejection from postmerger accretion disks (assuming that magnetic effects can only enhance it).

Despite awareness of broad agreement between groups carrying out viscous hydrodynamic simulations of NS merger disks, a quantitative code comparison has never been done. Experience from the core-collapse supernova modeling community shows that code comparisons help estimating the uncertainties of theoretical predictions and they can provide valuable insight into the physics of the system, by unfolding sensitivities with respect to specific assumptions and approximations adopted by individual codes or models [35–42].

Here we carry out a quantitative code comparison study between the viscous hydrodynamic setups of Just and collaborators (based on the ALCAR code; e.g. [16]) and Fernández and collaborators (based on a modified version of the FLASH code; e.g. [22]). Both setups have been used extensively over the past decade, and model viscous angular momentum transport, the BH pseudo-Newtonian potential, and the equation of state in a similar manner. The implementations differ primarily in the neutrino transport method employed (multigroup 2-moment [M1] for ALCAR, gray leakage + absorption for FLASH). For the comparison, we choose an initial condition with the same physical parameters, and vary the treatment of viscosity as well as the number of neutrino species and neutrino production processes considered. Each code employs production settings used previously in publications. Thus, while most of the settings are chosen to be the same between both codes, not all numerical details are exactly identical for this comparison study, such as the computational grid or the implementation of the equation of state. We study the role of the additional binding energy gained by the formation of heavy nuclei beyond alpha particles, which has been neglected in some accretion disk models, and can have a non-negligible impact on the outflow velocity. We also generate tracer particles and perform postprocessing nucleosynthesis calculations to assess the effects of code differences on *r*-process abundances, heating rates, and kilonova light curves. For the latter, we also explore how changing the number of particles included influences the light curves through the spatial distribution of lanthanides and actinides.

The structure of this paper is the following. Section II describes the codes used, approximations to the physics made, and the models evolved. Section III presents our results and analysis, followed by a summary and discussion in Sec. IV. The Appendix presents the equations used to determine the composition and internal energy assuming a mixture of neutrons, protons, alpha particles, and a representative heavy nucleus in nuclear statistical equilibrium (NSE).

II. METHODS

A. Codes and physics included

1. ALCAR

The ALCAR code [43], which is based on the magnetohydrodynamics code AENUS [44], evolves the viscous hydrodynamics equations along with conservation equations for the zeroth and first angular moments of the neutrino intensity (energy- and flux-density, respectively) on an axisymmetric spherical-coordinate mesh using finite-volume, high-order shock-capturing methods. ALCAR offers both a Newtonian and special relativistic framework, as well as various schemes for the time-integration, spatial reconstruction, and Riemann solver. Here we adopt the Newtonian version, a second-order Runge-Kutta integrator, the piecewise parabolic method (PPM_5) scheme of [45], and the Harten-Lax–van Leer Riemann solver, respectively. Gravity is treated using the pseudo-Newtonian Artemova-Novikov potential [46]. The equation of state (which was originally implemented in Ref. [47]) assumes a Boltzmann gas of four baryonic species (neutrons, protons, helium, and ^{54}Mn) in NSE, a Fermi-gas of electrons and positrons, and a thermal bath of photons. The radial domain of $r \in [10^6\ \mathrm{cm}, 4\times10^{11}\ \mathrm{cm}]$ is discretized by 576 logarithmically spaced zones, and the polar-angle domain, $\theta \in [0,\pi]$, is sampled by 160 uniform zones.

The ALCAR models presented in this study adopt the same setup as in [16], except that here we (a) include heavy-lepton neutrinos[1]; (b) evolve the entropy at radii beyond 1000 km (instead of evolving the sum of kinetic and thermal energy everywhere) in order to prevent numerical artifacts in the expanding ejecta once the thermal energy becomes subdominant; (c) start from slightly different initial conditions in the disk (constant entropy instead of polytropic relation with fixed maximum density); (d) use online tracers for the ejecta analysis (instead of postprocess tracers constructed via backward integration from the written output data). Despite these differences, the results for the ALCAR models discussed here are well in agreement with those in [16].

The neutrino transport adopts the M1 approximation, meaning that all higher angular moments (e.g., the Eddington tensor) appearing in the moment equations are expressed as local functions of the evolved moments using a closure relation. We adopt the closure by [48] (in the same form as in Ref. [43]). We discretize energy space of neutrinos using 10 energy bins logarithmically spaced between 0 MeV and 80 MeV and evolve the two-moment system for each energy bin. We take into account velocity-dependent terms up to first order in v/c following previous

[1]However, μ/τ neutrinos only play a subdominant role in BH-disks, at least in the case when neutrino oscillations are ignored (e.g., [30]).

disk studies (see, e.g., [8,16]). The transport follows the evolution of three neutrino species, ν_e, $\bar{\nu}_e$, and ν_x (with ν_x representing the four heavy-lepton neutrinos), which interact with free nucleons via emission and absorption (only ν_e and $\bar{\nu}_e$) as well as isoenergetic scattering, with rates taken from [49] and augmented by weak-magnetism corrections [50]. The production of heavy-lepton neutrinos proceeds through $e^{\pm}$ annihilation [51] and bremsstrahlung [52], while for the corresponding inverse processes we make use of the approximate detailed-balance treatment of [53]. Below densities of 10^8 g cm^{-3}, we turn off all pair-process related source terms in the neutrino moment equations, but, in order to still be able to follow energy- and momentum-deposition in the low-density polar funnels, we apply the corresponding source terms for pair annihilation in the hydro equations (see Ref. [54] for more details on their computation).

For each simulation, 10^4 equal-mass, passive tracer particles are initially placed in the disk, following the density distribution. The particles that exceed $r = 10^9$ cm are considered part of the outflow and set aside for postprocessing (cf. Sec. II B), with typically ~2000 outflow trajectories per model. All outflow particles remain within the computational domain for the duration of the simulations ($t = 10$ s).

2. FLASH

FLASH is a multiphysics simulation framework for astrophysical fluid dynamics [55,56]. To simulate long-term disk outflows in viscous hydrodynamics, we use the dimensionally-split PPM [57] solver, which is based on the PROMETHEUS code as implemented in FLASH version 3.2. The public version has been modified to allow for a nonuniform grid [58], inclusion of a viscous stress in axisymmetry [59], and the pseudo-Newtonian potential of Artemova [46] for gravity as reported in [23].

The neutrino implementation consists of a leakage scheme for cooling, with a local prescription to compute the optical depth using the pressure scale height [15,60]. Absorption is included using a light bulb-type scheme that accounts for the annular geometry of the accretion disk [22]. Three neutrino species are included $(\nu_e, \bar{\nu}_e, \nu_x)$, with the latter representing all four heavy lepton species. Charged-current weak interaction for emission and absorption reactions of $\{\nu_e, \bar{\nu}_e\}$ with nucleons are included using the rates of [49]. Additionally, neutrino emission from e^+e^- pair annihilation and plasmon decay is included, as well as opacity contributions from charged-current and neutral-scattering contributions following [61], as reported in [32].

The neutrino physics in the FLASH-based setup have been gradually improved over time, resulting in quantitative variations in the Y_e distribution of the outflow that nevertheless do not affect the results qualitatively. In [22], neutrino emission contained an exponential suppression of emission with optical depth. In [15], this was replaced by a leakage scheme that computed the production and diffusion times to modulate emission. In [60], separate mean energies were computed for electron neutrino and antineutrino absorption from the disk (previously only a single average energy was used for both species). Finally, since [32], the contributions of heavy lepton neutrinos are added in the leakage scheme, and the luminosity used for absorption in the next time step, computed from emission in the previous time step, is corrected by the power absorbed in the previous time step (this leads to the correct hierarchy of number luminosities of electron-type neutrinos and antineutrinos).

By default, the equation of state is that of [62], with the abundances of neutrons, protons, and alpha particles in NSE, accounting for the nuclear binding energy of alpha particles. An additional set of models is evolved with the same equation of state, but now additionally including a heavy nucleus (^{54}Mn) in nuclear statistical equilibrium, to capture the additional nuclear energy release and match the equation of state (EOS) used by ALCAR (see Sec. A in the Appendix).

The computational domain spans the radial range $[10^6, 10^{11}]$ cm and the full range of polar angles, using a logarithmic grid in radius with 640 cells, and a polar grid equispaced in $\cos\theta$ with 112 cells ($\Delta r/r \simeq \Delta\theta \simeq 0.02$ at the equator). The boundary conditions are outflow in radius and reflecting in polar angle.

FLASH models evolve tracer particles for postprocessing in same way as the ALCAR models; see Sec. II A 1.

B. Nucleosynthesis and kilonova postprocessing

We employ a nuclear reaction network that includes 7362 nuclei from nucleons to ^{313}Ds. We include α-decay, β-decay, charged particle reactions, neutron captures and their inverse process, photodisintegration, as well as spontaneous, neutron-induced, and β-delayed fission. It corresponds to the set of nuclear reactions labeled 'FRDM' in Ref. [63]. We also consider weak interactions including the electron/positron captures and (anti)neutrino absorption on nucleons.

For all trajectories, the nucleosynthesis calculation is started from the last time when the temperature reaches 10 GK. For each tracer the early evolution history of thermal quantities and weak interaction rates in the trajectory is obtained based on the simulation data. When the disk simulation ends at $t_f = 10$ s, the tracer reaches a radius r_f. After the end of simulation we take the assumption of homologous expansion such that the density is extrapolated as $\rho(t) = \rho(t_f)[1 + v_f(t - t_f)/r_f]^{-3}$ with the asymptotic velocity v_f at t_f. The temperature is evolved consistently, taking into account viscous and nuclear heating, and including the energy exchange associated with emission and absorption of neutrinos.

Using the masses and final (i.e., at $t = t_f$) velocities of all trajectories, as well as the nuclear heating rates, mass fractions of lanthanides and actinides, and average mass numbers along each trajectory, we estimate the kilonova signal using the approach detailed in [64]. The effective heating rates powering the kilonova are computed from the total heating rates using the approximate thermalization efficiencies of Ref. [65]. In addition to heating from β^-- and α-decays as well as fission, which is treated following the standard treatment of [65] (as done in Ref. [64]), we find also a small contribution of e^--capture and β^+-decays (see, e.g., Ref. [66]) that are dominated by the decay of ^{56}Ni, for which 80% (20%) of the energy goes into γ-rays (neutrinos). In contrast to the multidimensional kilonova analysis of [64], we assume spherical symmetry, as we are only interested in the most basic properties of the kilonova signal. To this end, we do not apply kernel-based interpolation techniques to map the trajectory properties to the velocity grid, but instead use simple zeroth-order binning as follows. We discretize the velocity range between $v/c = 0$ and 0.5 using 50 bins and, for each velocity bin ranging from v to $v + \Delta v$, obtain its mass Δm by summation of all trajectories falling in this velocity range. The heating rates, lanthanide mass fractions, and average mass numbers (needed for the calculation of the gas energy density) for this bin are computed as mass-weighted averages over the same trajectories. The approximate radiative transfer equations are then solved on a finer grid (ranging from $v/c = 0$ to 0.6 with 300 uniform zones) using linear interpolation to map from the coarser grid.

C. Model parameters

The baseline configuration mirrors the parameters of model *m1* of [30], which has a black hole of $3M_\odot$ and spin parameter of 0.8. The initial condition for the disk is an equilibrium torus with mass $0.1M_\odot$, constant initial $Y_e = 0.1$, constant entropy of 8 k_B per baryon, constant specific angular momentum, and radius of initial density maximum at $r = 40$ km. This equilibrium initial condition is chosen to compare with previously published models and to facilitate analysis. A disk formed self-consistently in a dynamical merger is expected to have a distribution of electron fractions, entropies, and angular momenta, and the resulting outflow may differ from that obtained when using an equilibrium torus (e.g., [24,31,67,68]). The kinematic viscosity coefficient follows the functional form of [69]; namely,

$$\nu = \alpha \frac{c_i^2}{\Omega_K}, \tag{1}$$

where α is a constant, $c_i = \sqrt{p/\rho}$ is *the isothermal sound speed*, with p the gas pressure and ρ the mass density, and Ω_K is the equatorial Keplerian angular velocity of the pseudo-Newtonian potential. The default model has $\alpha = 0.06$, and we also consider alternative models with $\alpha = 0.03$. Only the $r\phi$ and $\theta\phi$ components of the viscous stress tensor are considered, in order to mimic conversion of shear kinetic energy into thermal energy by turbulent angular momentum transport driven by the magnetorotational instability [70].

Our naming convention prepends the letter "A" to models run with ALCAR, and "F" to models run with FLASH. Models named *full* use the entire production settings of each code as described in Sec. II A, with suffixes $\{a3, a6\}$ when using $\alpha = \{0.03, 0.06\}$, respectively.

In addition, we evolve a set of models with reduced neutrino physics; no heavy lepton neutrinos, and only charged-current neutrino/antineutrino emission and absorption, and neutral-current scattering on nucleons. These models are denoted with 'red' (for reduced).

Also, a version of all models is repeated in FLASH, but now including a representative heavy nucleus (^{54}Mn, see Appendix) in the EOS, to match that used in ALCAR. These models start with 'Fh' (for heavy nucleus).

Finally, model F-full-a3 is repeated using 10 times more tracer particles than the default value, to test convergence of particle-based analyses (we name it F-full-a3-N10).

III. CODE COMPARISON RESULTS

A. Dynamics

1. Accretion

The evolution of the disk during the first ~100 orbits at the radius of initial density maximum (~300 ms) is mostly laminar, and set by the interplay between viscous angular momentum transport and neutrino cooling. Figure 1 shows the mass accretion rate at $r = 10$ km, slightly inside the radius of the innermost stable circular orbit (ISCO) ~13 km for all models evolved. Aside from a small offset in time, the evolution of the accretion rate is nearly identical for ALCAR and FLASH models during this initial phase.

Around ~100 orbits, with the exact value determined by the strength of viscosity, neutrino cooling decreases sharply and the disk becomes radiatively-inefficient. The timing of this transition at ~200 ms and ~450 ms for $\alpha = 0.06$ and 0.03, respectively (Fig. 2), shows excellent agreement between ALCAR and FLASH models. Combined with the similarity of the inner accretion rate evolution, this agreement shows that the viscous angular momentum transport is fully compatible between the two implementations.

After the transition to the radiatively inefficient (advective) phase, the disk becomes highly turbulent and the mass accretion rate at the ISCO becomes more stochastic. Figure 1 shows that the amplitude of fluctuations and overall evolution in accretion rate remains consistent between ALCAR and FLASH models. At this stage, a small offset becomes apparent between FLASH models that differ in the inclusion of the nuclear binding energy of a representative heavy nucleus (models F and Fh in Fig. 1),

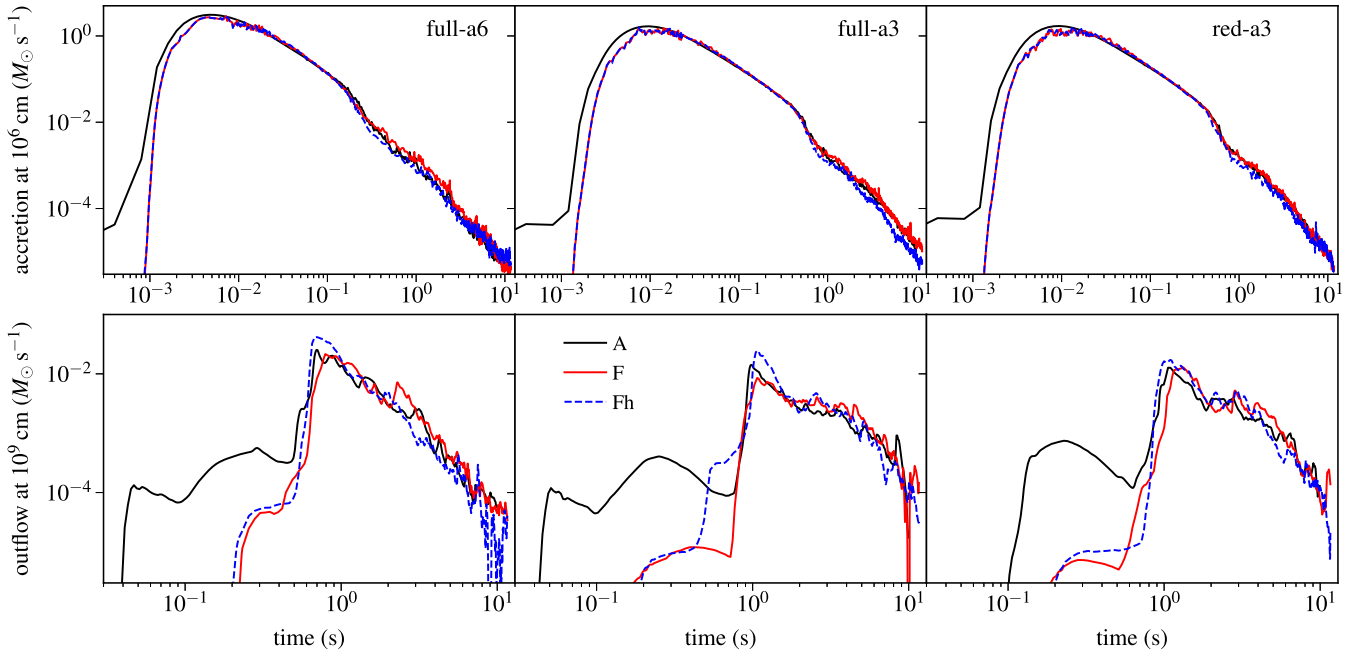

FIG. 1. Mass accretion rate at $r = 10$ km (top) and total mass outflow rate at $r = 10^9$ cm (bottom), for various models, as labeled for each column (see Table I for details). The offset in the accretion rate at early times between ALCAR and FLASH models is due to the initial condition and density floor values, which are not identical (despite the initial disk having the same physical parameters, see Sec. II C). The bump in the ALCAR model outflow at $t \sim 200$–400 ms corresponds to the neutrino-driven wind, which we attribute to stronger neutrino absorption in the M1 scheme relative to the light bulb prescription used in FLASH.

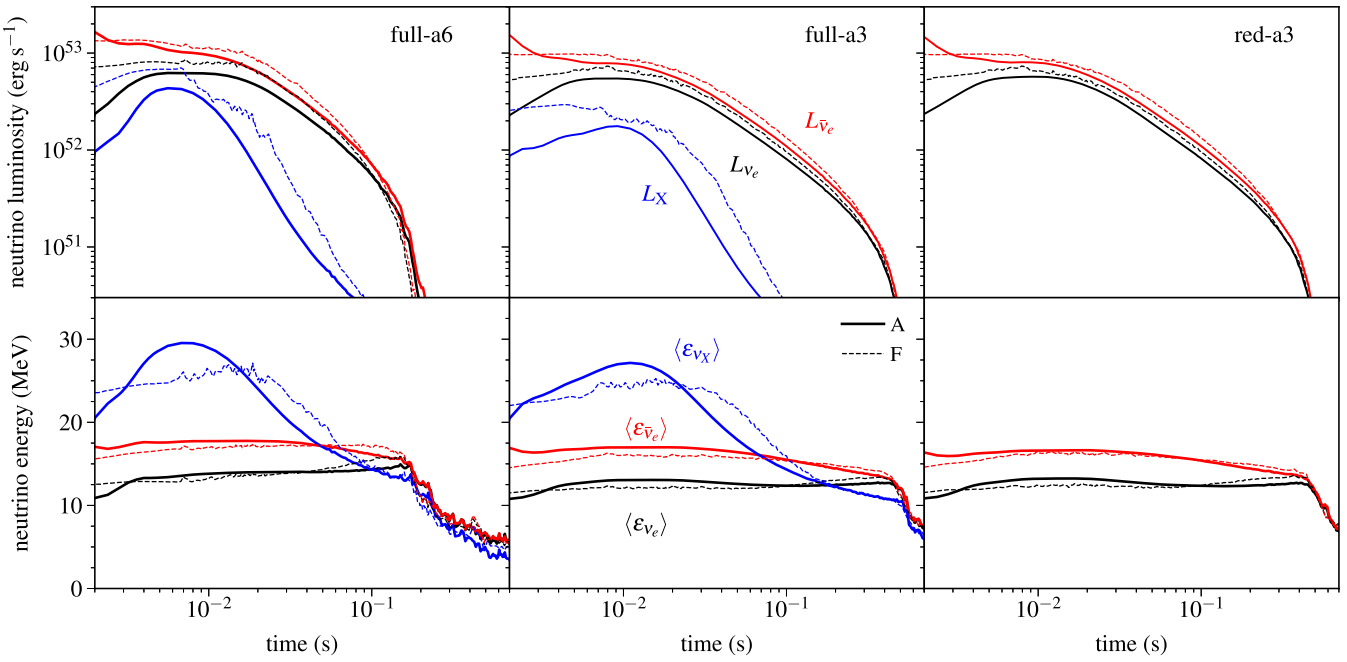

FIG. 2. Neutrino luminosities (top) and mean neutrino energies (bottom), for various models, as labeled for each column. Quantities for A-models (ALCAR, solid lines, M1 neutrino scheme) are measured at $r = 500$ km, with luminosities computed from the radiative flux evolved with the M1 scheme. For F-models (FLASH, dashed lines, leakage + light bulb neutrino scheme) luminosities are computed as the sum of the (leakage-corrected) emissivities over the entire domain, corrected for absorption, hence the higher level of variability relative to A-models. The heavy lepton luminosity includes the contribution from all four species. F-models do not include the nuclear binding energy of a heavy nucleus.

TABLE I. Models evolved and summary of results. The first three columns from the left show model name (A: ALCAR, F: FLASH with no heavy nucleus in the EOS, Fh: FLASH with ^{54}Mn), Shakura-Sunyaev viscosity parameter, and whether the standard neutrino species and emission processes for each code are used (No = reduced to $\{\nu_e, \bar{\nu}_e\}$, with charged-current and neutrino-nucleon scattering processes only). The following two columns show total mass ejected at $r = 10^9$ cm as measured from the grid, and from tracer particles, respectively, as well as average velocity from tracer particles at the same radius. The last four columns show average quantities at the last position/time where the temperature is 5 GK in each trajectory; electron fraction, entropy, radius, and expansion time (the latter computed as average radius over average radial velocity at 5 GK).

Model	α	All ν?	$M_{\rm ej,grid}$ ($10^{-2}M_\odot$)	$M_{\rm ej,part}$ ($10^{-2}M_\odot$)	$\langle v_r\rangle_{\rm r9}$ (10^{-2} c)	$\langle Y_e\rangle_{5\ \rm GK}$	$\langle S\rangle_{5\ \rm GK}$ (k_B/b)	$\langle r\rangle_{5\ \rm GK}$ (10^7 cm)	$\langle t_{\rm exp}\rangle_{5\ \rm GK}$ (ms)
A-full-a6	0.06	Yes	1.87	1.81	4.19	0.256	19.0	6.33	75
F-full-a6			2.06	2.12	3.73	0.283	19.4	6.96	79
Fh-full-a6			2.26	2.30	4.27	0.279	17.4	7.31	77
A-full-a3	0.03	Yes	1.54	1.50	3.56	0.277	20.0	5.56	98
F-full-a3			1.67	1.67	2.87	0.298	20.0	6.57	102
Fh-full-a3			1.91	1.88	3.27	0.289	18.6	6.78	101
A-red-a3	0.03	No	1.62	1.57	3.39	0.283	19.8	5.55	94
F-red-a3			1.82	1.81	2.70	0.301	19.6	6.76	97
Fh-red-a3			1.98	1.96	3.17	0.291	18.4	6.75	108

with the models having a larger nuclear binding energy release showing a larger drop in accretion rate (an effect first reported in [71]).

2. Outflow kinematics and nuclear energy release

While the bulk of mass ejection in viscous hydrodynamic evolution takes place once the disk becomes radiatively inefficient, earlier outflows do occur. Figure 1 shows the total mass outflow rate (bound and unbound) at 10^9 cm for all models. The most notable difference between ALCAR and FLASH models is the early bump at 200–400 ms, which corresponds to mass ejection driven by neutrino energy deposition (the 'neutrino-driven wind').[2] This early outflow component is significantly larger in the ALCAR models, which implement multigroup M1 neutrino transport. Unsurprisingly, the accuracy of neutrino-driven mass ejection is dependent on the quality of the neutrino transport approximation.

Mass ejection following the transition to radiative inefficiency peaks at a time ∼1 s at the extraction radius located at 10^9 cm (Fig. 1). The rise, peak, and subsequent evolution of this component, which makes up the majority of the disk wind, is similar yet quantitatively different for ALCAR and FLASH models.

While identical evolution is not expected given the large stochatic fluctuations, a systematic difference is observed: both ALCAR and FLASH models with a heavy nucleus (Fh) rise earlier to peak, reach a higher peak, and decrease faster thereafter relative to the FLASH models (F) that only include the nuclear binding energy of alpha particles. Table I shows that this difference translates into a ∼10% boost in ejected mass and a 10–20% boost in average outflow velocity when comparing models F and Fh, which only differ in the inclusion of the nuclear binding energy of ^{54}Mn. Compared to ALCAR models, F models have all lower average velocity but eject more mass.

To illustrate the magnitude of the nuclear energy release in the different EOS mixtures, we plot in Fig. 3 the NSE abundances for a representative thermodynamic path of the outflow ($Y_e = 0.3, \rho \propto T^3$). At low temperature, the difference in nuclear binding energy released per nucleon between the Fh (^{54}Mn) and F (^{4}He only) models is

$$(0.648 \times 8.74\text{–}0.6 \times 7.07)\ \text{MeV} \simeq 1.4\ \text{MeV}. \quad (2)$$

If fully converted to kinetic energy, this would correspond to a specific kinetic energy of 2.9×10^{-3} c^2. For an initial velocity of 0.035 c, the additional kinetic energy would boost the ejecta to 0.065 c. The difference in expansion velocity at 10^9 cm between F and Fh models (∼0.005 c) is much smaller than this value, however, indicating that most of this additional nuclear energy released remains as thermal energy at least up to this radius.

The outflow velocity distribution is shown in the rightmost column of Fig. 4. In all cases, the velocity distribution has the same qualitative form; a double-peaked structure, a sharp cutoff at ∼0.1 c, and an extended tail to lower velocities. The distribution shows excellent agreement between all models that use $\alpha = 0.03$ (full-a3 and red-a3), with quantitative differences related to the amount of mass ejected. A more noticeable difference appears in the full-a6 set, for which model Fh shows low-velocity tail that is shifted to higher velocities. This is consistent with the larger average velocity shown in Table I which is due to less

[2]Note that there is a finite travel time for outflow material to reach the extraction radius from the region where it is launched; 10^9 cm/0.1 c ∼ 0.3 s.

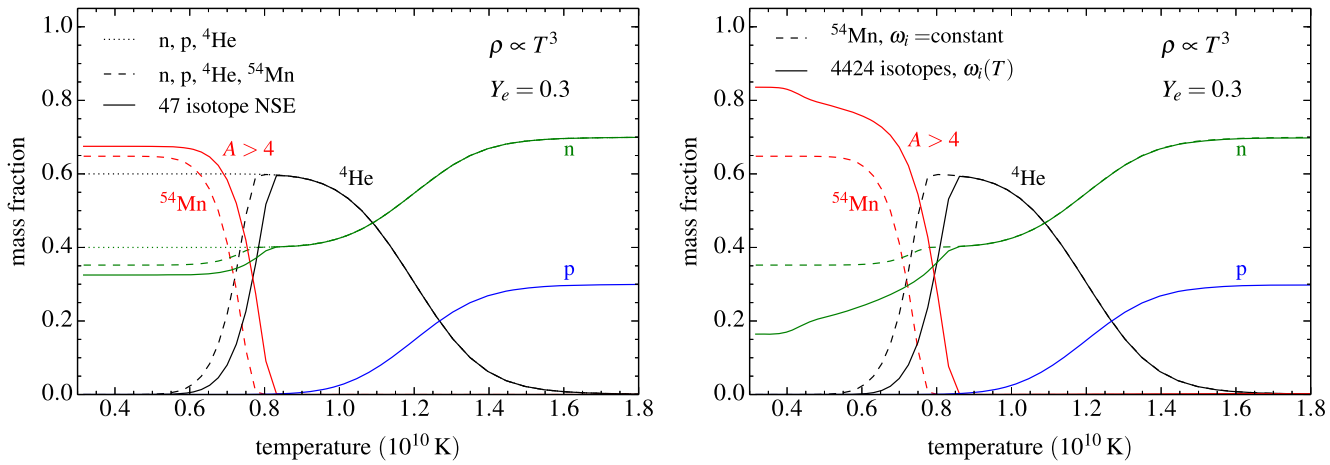

FIG. 3. *Left:* Abundances in NSE as a function of temperature, for three different mixtures: neutrons protons and alpha particles (dotted lines), adding ^{54}Mn as the only heavy nucleus (dashed), and the 47 isotope NSE mixture of [72] (solid lines). The NSE equations are solved with constant partition functions, as in Appendix. The electron fraction and thermodynamic path are chosen to be representative of the disk outflow ($\rho \propto T^3$, with $T = 3 \times 10^8$ K at $\rho = 2000$ g cm^{-3}). F models use an EOS without a heavy nucleus (dotted lines), while Fh and A models use ^{54}Mn as a representative heavy nucleus. The red solid curve contains the mass fractions of all nuclei heavier than ^{4}He, the asymptotic value at low temperature is 0.675. For the dashed line, this value is 0.648. *Right:* Same as in the left panel, now comparing the same mixture with ^{54}Mn and constant partition functions as in the left panel (dashed lines), with a mixture of 4452 isotopes that uses temperature-dependent partition functions in the NSE equations (solid lines). The asymptotic value of the solid red curve at low temperature is 0.836.

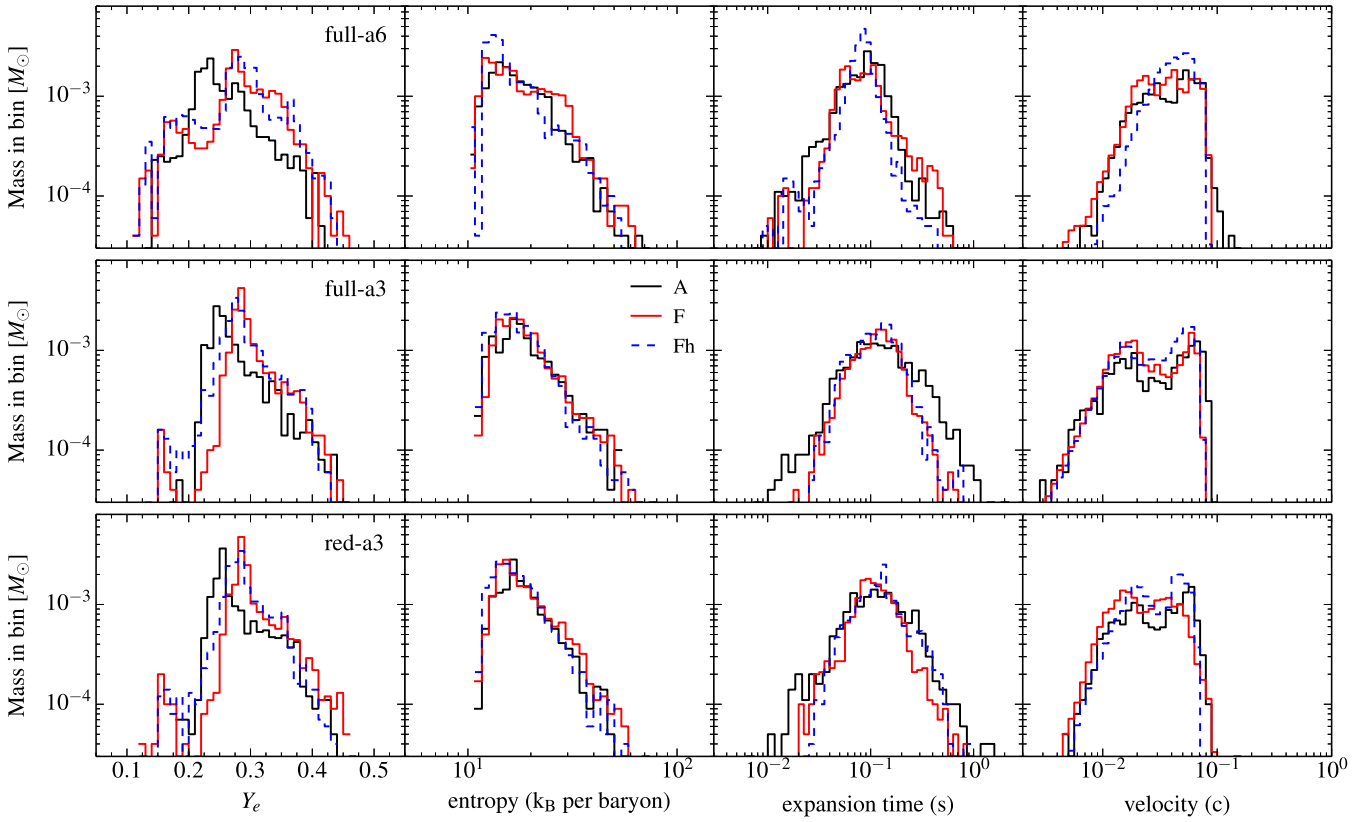

FIG. 4. Mass histograms as a function of various quantities, for the three different model configurations we explore, as labeled for each row. Quantities are computed from tracer particles that are ejected past $r = 10^9$ cm by the end of the simulation at $t = 10$ s. The electron fraction Y_e, entropy, and expansion time $t_{\rm exp} = r/v_r$ are computed at the last time a particle reached $T = 5$ GK. For the latter, we only include particles with positive velocity. The velocity histogram is computed at $r = 10^9$ cm.

material moving at low speeds. Overall, ALCAR and FLASH models that include the nuclear binding energy contribution from ^{54}Mn (Fh) have average velocities that differ by less than 10%, thus accounting for most of the difference between A and F models.

Figure 3 also shows abundances as a function of temperature for two NSE mixtures with more nuclei. Using the 47 isotope mixture of [72] and employing constant nuclear partition functions ω_i, results in a marginally higher abundance of heavy nuclei (everything other than ^{4}He, n, p) by 4% relative to using only ^{54}Mn, with an increase in the nuclear energy release of the same magnitude. Significant differences require a much larger number of isotopes; the right panel of Fig. 3 shows abundances obtained with a mixture of 4,452 isotopes and using temperature-dependent partition functions $\omega_i(T)$. While the effect of the temperature-dependent partition functions is to shift the transition between nuclear species to slightly higher temperature relative to the case of constant partition functions, the larger number of nuclei allows to reach a higher mass fraction and consequently larger nuclear energy release. The 20% increase in heavy nuclei mass fraction results in an extra ∼1.7 MeV per nucleon released. In terms of additional kinetic energy when fully converted, and relative to using only ^{54}Mn as a representative nucleus and 0.035 c as a baseline velocity when only including alpha particles, this extra nuclear energy release would boost the outflow from 0.065 c to 0.088 c. This motivates future work toward improving how nuclear physics and *r*-process heating is included in postmerger simulations.

3. Neutrino quantities and equilibrium Y_e

The neutrino luminosities and mean energies for A- and F-models are shown in Fig. 2. In ALCAR, the M1 luminosities are measured at 500 km, whereas in FLASH they are computed instantaneously in the entire domain, correcting for the neutrinos absorbed, as in [32]. Despite the different transport methods, the global electron-type neutrino and antineutrino luminosities after $t \sim 3$ ms are consistent in both codes to within 10–20%, regardless of the neutrino physics included (i.e., model full-a3 versus red-a3). A larger discrepancy of up to a factor ∼2 is obtained in the heavy-lepton luminosities (models full-a6 and full-a3). Nevertheless the time evolution is remarkably close in all species, owing to the agreement in angular momentum transport and global dynamics as discussed in Sec. III A 1.

Figure 2 also shows the mean energies for all neutrino species evolved, obtained as the global ratio of energy- to number luminosities for each species (as in [61]). For electron-type neutrinos and antineutrinos, the mean energies show close similarity as with the luminosities, with no significant differences in the level of agreement between models that include all neutrino interactions and those that reduce the neutrino emitting channels. Again, a larger discrepancy is observed in the mean energies of heavy lepton neutrinos.

The electron fraction distribution of the outflow at $T = 5$ GK (Fig. 4) shows a systematic shift of its peak toward lower electron fractions by ∼0.02–0.03 in ALCAR models relative to FLASH models, consistent with the offset in average Y_e shown in Table I. The entropy distribution peaks at lower values in FLASH models, but shows otherwise a similar shape relative to ALCAR models, consistent with the agreement in mean values (Table I). The expansion time also shows consistent distributions between FLASH and ALCAR models, with larger deviations in Fh models relative to both F and A models.

We can analyze the offset in Y_e by computing the equilibrium values toward which weak interactions are driving the composition in the disk. These equilibrium values are obtained by balancing the rates of neutrino and antineutrino emission/absorption (as in, e.g., Ref. [8]). We denote by $\langle Y^{\rm eq}_{\rm e,em}\rangle$ the mass-averaged equilibrium electron fraction obtained by balancing electron neutrino and antineutrino emission rates, $\langle Y^{\rm eq}_{\rm e,abs}\rangle$ the corresponding equilibrium value obtained with absorption rates only, and $\langle Y^{\rm eq}_{\rm e,tot}\rangle$ the equilibrium value obtained by balancing both emission and absorption rates.

Figure 5 shows the evolution of the mass-averaged electron fraction $\langle Y_{\rm e}\rangle$ and the total equilibrium value towards which weak interactions are driving it. At early times, these equilibrium values are moderately neutron rich (∼0.2), consistent with the mild electron degeneracy of the disk (also shown in Fig. 5). The offset at $t = 0$ in equilibrium Y_e and electron degeneracy parameter is due to the different treatment of the ion entropy in each EOS. In FLASH, the entropy of ions is obtained by assuming that they are a single species with average mass number $\bar{A}$ and adiabatic index $5/3$, ignoring the statistical weight g (spin degree of freedom), see Eq. (110) in Ref. [55]. Since both protons and neutrons have $\bar{A} = 1$, they are treated as the same species and thus, in addition to ignoring the difference between their masses, the 'entropy of mixing' (terms of the form $Y_i \ln(Y_i)$, with Y_i the number fraction) is absent. In ALCAR, the ion entropy is computed as the sum of individual entropies from the different species considered, and including statistical weights ($g = 2$ for nucleons and $g = 1$ for nuclei). This results in a difference of ∼1 k_B per baryon in total entropy between the two EOSs for a given $\{\rho, T, Y_e\}$ combination characteristic of the initial torus density maximum. Since both codes start from equilibrium tori constructed with an entropy of 8 k_B per baryon, the thermodynamic conditions have a small initial offset.

As the disk density decreases and degeneracy drops, weak equilibrium increases Y_e toward ∼0.5 because free nucleons recombine into α particles and heavy nuclei (characterized by an average mass number $A_{\rm h}$ and charge number $Z_{\rm h}$). Assuming full recombination and a fixed representative heavy nucleus, mass and charge conservation lead to the

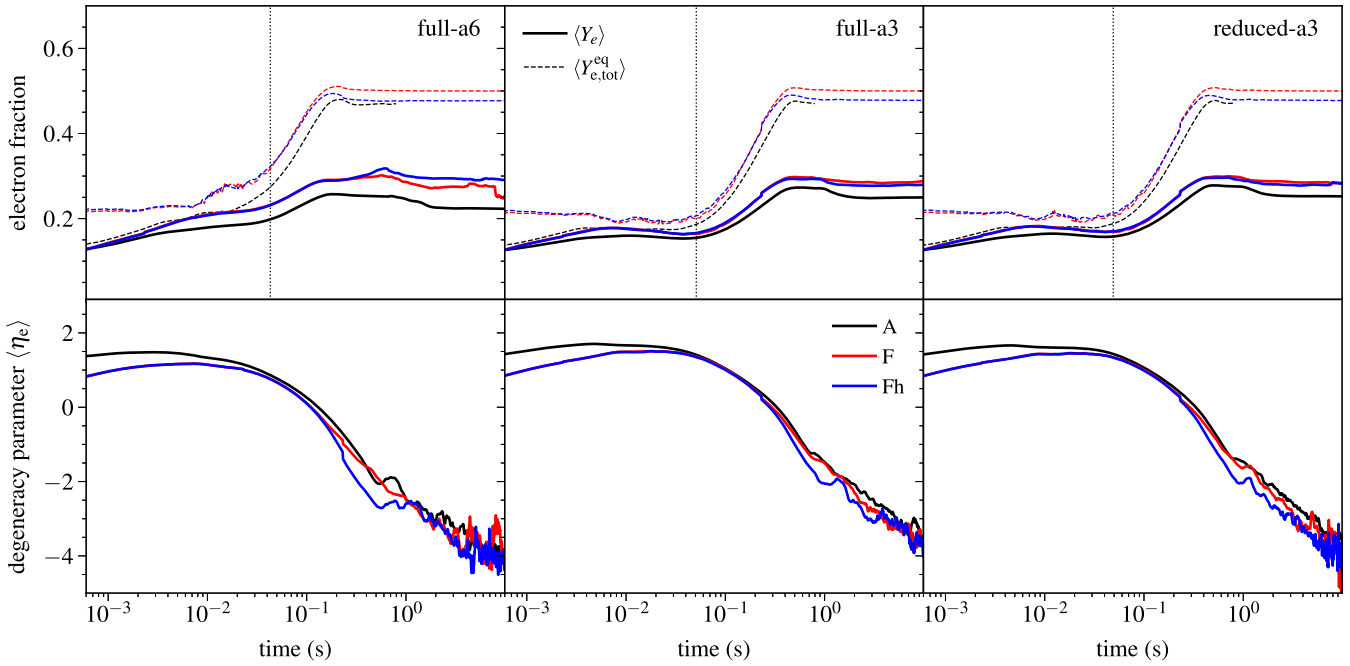

FIG. 5. *Top:* Mass-averaged electron fraction (solid lines) and mass-averaged equilibrium electron fraction in the disk, considering both emission and absorption (dashed lines). The average considers matter that satisfies $T > 0.1$ MeV, $\rho > 10^3$ g cm^{-3}, and $r < 10^9$ cm. The vertical dotted line indicates the time at which L_{ν_e} drops by a factor of 3 from its maximum value in ALCAR models (cf. Fig. 2). *Bottom:* Mass-averaged electron degeneracy parameter, excluding rest mass. Note that, while the initial condition in ALCAR and FLASH models has the same physical parameters, it is constructed independently using slightly different equations of state, which accounts for the initial offset in equilibrium Y_e and degeneracy parameter.

following relation for the asymptotic equilibrium electron fraction at low temperature:

$$Y_e^{\rm eq} = \frac{1}{2} - \left[\frac{1}{2} - \left(\frac{Z_{\rm h}}{A_{\rm h}}\right)\right] X_{\rm h}, \tag{3}$$

where Eq. (3) is also valid in the case where $X_{\rm h}$, $A_{\rm h}$, and $Z_{\rm h}$ denote the (average) properties of a distribution of heavy nuclei.

Consistent with these considerations, both ALCAR models and FLASH models that assume ^{54}Mn as representative heavy nucleus have on average $X_{\rm Mn} \sim 0.6$ at late times, i.e., $Y_e^{\rm eq} \simeq 0.48$, that corresponds to the asymptotic average $\langle Y_e^{\rm eq} \rangle$ at low temperatures. FLASH models without ^{54}Mn, i.e. only α particles, have $Y_e^{\rm eq} = 0.5$ (Fig. 5).

The mass-averaged electron fraction follows the shape of the equilibrium value without reaching it in both ALCAR and FLASH models, decoupling around the time at which neutrino luminosities drop significantly (cf. Fig. 2). An offset between ALCAR and FLASH models is apparent in both the average electron fraction and the equilibrium value, with FLASH models showing consistently higher values. The offset in the electron fraction distribution seen in Fig. 4 thus most likely originates from the offset in the equilibrium electron fractions obtained with each code, given that all models start with the same initial electron fraction.

To analyze this offset further, we separate the equilibrium electron fraction into emission and absorption components in Fig. 6 for the full-a3 models. At early times, the ALCAR model has a lower emission equilibrium and a higher absorption equilibrium than FLASH models, such that the net equilibrium value is lower. The difference in

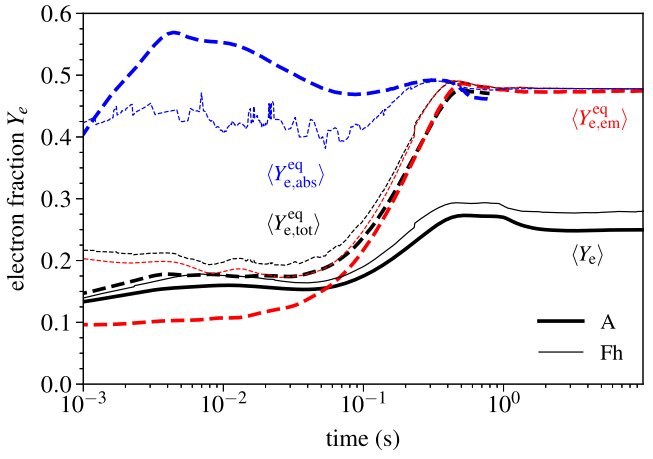

FIG. 6. Mass-averaged electron fraction (solid lines) and equilibrium electron fractions (dashed lines), as labeled, for models A-full-a3 (thick lines) and Fh-full-a3 (thin lines).

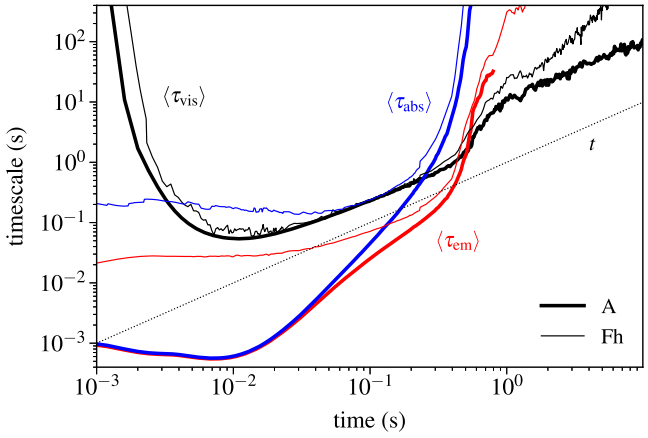

FIG. 7. Characteristic timescales governing the evolution of Y_e in the disk for full-a3 models (ALCAR: thick lines, FLASH: thin lines). Shown are the weak interaction timescale due to neutrino emission $\langle\tau_{\rm em}\rangle$ and absorption $\langle\tau_{\rm abs}\rangle$, and viscous (accretion) timescale $\langle\tau_{\rm vis}\rangle$, all computed as in Ref. [8]. The dotted line denotes the current time t.

emission equilibrium can be attributed to the higher electron degeneracy in the ALCAR models (Fig. 5), while the difference in absorption equilibrium is likely due to the different neutrino transport implementations.

Note that the average Y_e in FLASH models takes longer to approach the equilibrium electron fraction than in ALCAR models, because the effective weak interaction timescales are significantly longer due to the leakage and absorption implementation. Figure 7 shows the average weak interaction timescales in the disk due to neutrino emission $\langle\tau_{\rm em}\rangle$ and absorption $\langle\tau_{\rm abs}\rangle$, as well as the accretion (viscous) timescale $\langle\tau_{\rm vis}\rangle$, for the full-a3 model, computed as in Ref. [8]. In the ALCAR model, the emission and absorption timescales are shorter than the accretion and current times t, hence the torus approaches Y_e equilibrium quickly and remains close to that state until freeze-out, as shown in Fig. 6. The FLASH model, on the other hand, is such that the shortest timescale, $\langle\tau_{\rm em}\rangle$, is initially shorter than the accretion time but longer than the current time, hence the Y_e of the torus remains out of equilibrium until $t \sim 10$ ms.

As time elapses and the absorption contribution decreases, the net equilibrium Y_e merges with the emission equilibrium, and the offset in equilibrium value between the two codes decreases. Despite these differences, the actual mass-averaged electron fraction between the two codes has a moderate offset of ∼0.02 throughout the evolution.

B. Nucleosynthesis

Figure 8 compares the abundance yields from ALCAR and FLASH models as functions of mass number A at 1 Gyr and of atomic number Z at 1 day. The abundance patterns in

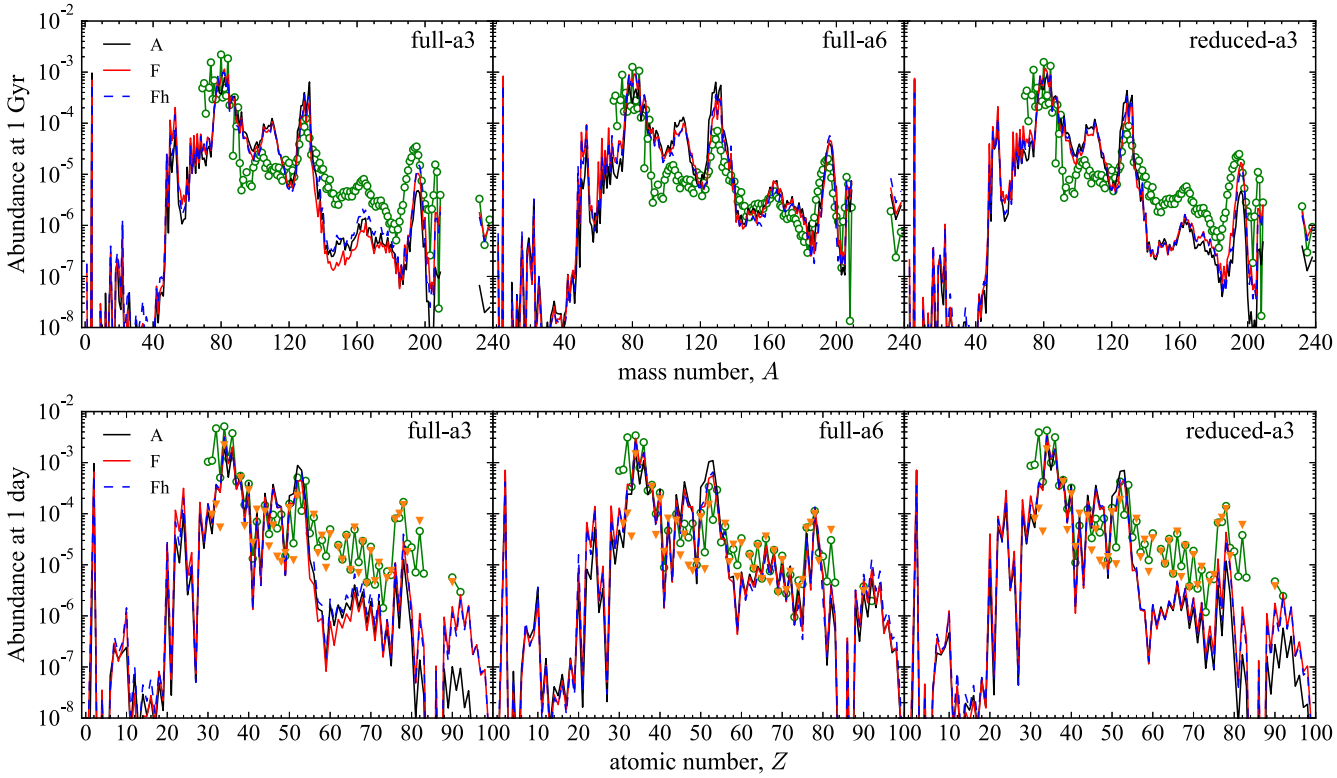

FIG. 8. Abundance yields as functions of mass number A at 1 Gyr (top row) and atomic number Z at 1 day (bottom row). Green circles show the solar r-process abundances [73] and are scaled to the yields of Sr in the ALCAR models. Orange triangles in the lower row show abundances observed for the metal-poor star HD-222925 [74] and are scaled to the solar Eu abundance.

models F and Fh are very similar to each other, except that lanthanides are enhanced by a factor of ∼2–4 in model Fh-full-a3 compared to model F-full-a3. This suggests that the nucleosynthesis outcome is not very sensitive to the inclusion of the nuclear binding energy of ^{54}Mn (Fh).

Overall, ALCAR and FLASH models agree very well. The abundance patterns near the first r-process peak are well reproduced compared to that in the metal-poor star HD-222925 [74]. Consistent with the offset for the peak electron fraction from ∼0.28–0.29 in the FLASH models to ∼0.23–0.24 in the ALCAR models (Fig. 4), the abundances of 2nd-peak r-process elements ($A \approx 130$) in the ALCAR models are higher than in the F and Fh models, namely by a factor of ∼1.5–2, because those elements are most efficiently produced from the ejecta with $Y_e = 0.2$ to 0.23. The enhancement of ^{132}Te at 1 day leads to higher specific heating rates (shown in the second column of Fig. 9) originating from the β^- decay chain of ^{132}Te–^{132}I–^{132}Xe. A noteworthy difference is observed in the abundance of actinides, which is about a factor of 10–40 smaller in the ALCAR models, associated with the lack of very neutron-rich ejecta with $Y_e < 0.2$ in these models. The small amount of ejecta with $Y_e \sim 0.1$ in FLASH models (Fig. 4) is apparently sufficient to make a significant difference in the yields of actinides, therefore potentially allowing these elements to be used as diagnostics of the ejecta electron fraction.

The model sets full-a3 and red-a3 underproduce nuclei with $A > 140$ compared to the solar r-process pattern, while the model set full-a6 shows a more consistent abundance pattern even in third-peak elements and actinides. As found in previous studies (e.g., [8,16,22]), a higher viscosity leads to faster matter ejection and, therefore, earlier freeze-out of Y_e, increasing the fraction of matter ejected with $Y_e < 0.2$ (i.e., neutron-rich enough to enable actinide production). The early freeze out results in more matter being ejected with $Y_e < 0.2$, leading to a more solar-like distribution of elements heavier than $A \approx 140$ [8].

C. Kilonova signal

The kilonova signal produced by the ejecta is compared for all models in Fig. 9. As anticipated from the similarity of outflow properties and nucleosynthesis yields, the basic kilonova properties (bolometric luminosity, photospheric temperature and velocity) show an overall good level of agreement, especially considering

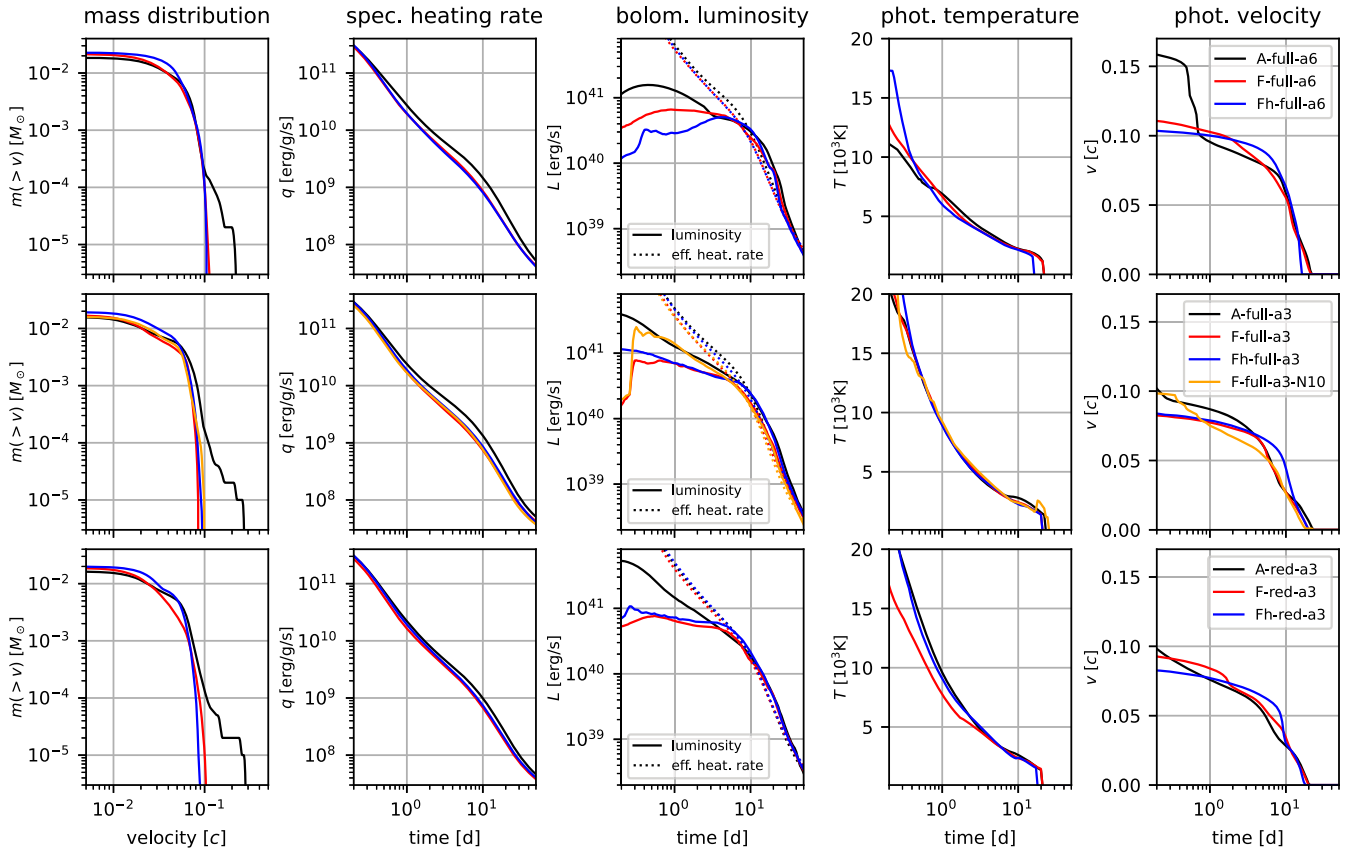

FIG. 9. Basic kilonova properties, namely, from left to right, the mass distribution (i.e. for given v the mass of material faster than v), the specific heating rate (before thermalization and including neutrino contributions), bolometric luminosity (solid lines) and total effective heating rates (dotted lines), photospheric temperature, and photospheric velocities. The last two quantities are computed as in Eqs. (28) and (29) of [64]. Each row shows results for the models listed in the right panel.

that matter ejection from turbulent disks involves a non-negligible level of stochasticity.

The specific heating rates, shown in the second column from the left, differ only marginally when varying the physics input, while they are systematically shifted to higher values (about 20–40% during the considered times) in the ALCAR models compared to the FLASH models. This difference is connected to the more pronounced second r-process peak in the ALCAR models, as mentioned in the previous section. However, the impact of this difference on the brightness of the kilonova is partially compensated by the slightly smaller ejecta masses of the ALCAR models.

Since BH-disk ejecta are relatively slow compared to other ejecta components that can be produced in a NS merger, they become optically thin at rather late times, $t \sim 5$–10 d. These transition times when the ejecta start to become optically thin can be read off in the third column of Fig. 9 as the times when the total luminosities for the first time exceed the effective heating rates. Previous to these transition times, most of the ejecta are still optically thick and the emission is produced from just the outermost ejecta layers (see first and fifth column of Fig. 9). The higher luminosities seen at early times in the ALCAR models are likely to be connected to the more pronounced neutrino-driven mass ejection in the ALCAR models, which leads to an extended high-velocity tail.

However, another, purely numerical reason may also be poor sampling of the high-velocity edge of the ejecta with tracer particles. This is suggested by the comparison with model F-full-a3-N10, which evolves 10 times more tracer particles than model F-full-a3 and exhibits significantly brighter emission at early times. This comparison suggests that the adopted number of 1500–2000 equal-mass tracer particles is high enough to describe the main part of the light curve, during which the photosphere travels through the ejecta, but is insufficient for accurately resolving the emission at earlier times. We note, however, that the reduced accuracy at early times may not be overly relevant for kilonova modeling of NS mergers, because the early light curve is likely to be dominated by other ejecta components.

IV. SUMMARY AND DISCUSSION

We have carried out a code comparison study of ALCAR and FLASH, both of which have been used extensively over the past decade to study the viscous hydrodynamic evolution of BH accretion disks formed in neutron star mergers. For the comparison, we employ a representative system around a BH with identical initial conditions, and vary the viscosity parameter as well as neutrino physics. Our main results are the following:

(1) We find excellent agreement in the quantities that depend on angular momentum transport, i.e., the accretion rate history, and timing of weak interaction freeze-out (Figs. 1 and 2). A larger discrepancy is obtained in quantities that depend on the neutrino transport approximation, such as the magnitude of the neutrino-driven wind (Fig. 1) and the electron fraction distribution of the ejected material (Fig. 4);

(2) Both codes show the same progression of the equilibrium electron fraction from low to high values as the disk becomes less degenerate over time. Slightly higher electron degeneracies, and therefore more neutron-rich equilibrium conditions, are found in the ALCAR models, which accounts for the $\sim$10% shift to lower average Y_e values in the ejecta of the ALCAR compared to the FLASH models (Figs. 5 and 6);

(3) The outflow velocity is sensitive to the accuracy with which the nuclear binding energy release is treated. Including a representative heavy nucleus (^{54}Mn) results in an additional energy release of $\sim$1 MeV per baryon relative to including only alpha particle recombination (Fig. 3). Additional energy release can be obtained when including a much larger isotope mixture. This motivates further work toward including more realistic nuclear physics in post-merger simulations;

(4) The nucleosynthesis yields follow the offset in Y_e, with ALCAR models producing more elements with $A > 130$ by a factor $\sim$2 relative to FLASH models, within an overall good agreement otherwise. This also results in a higher heating rate in ALCAR models due to enhancement of the ^{132}Te–^{132}I–^{132}Xe β^- decay chain. Very minor differences result from the additional energy release from ^{54}Mn models in FLASH (Fh versus F), with the possible exception of factor $\sim$2 changes in the lanthanides fraction in some models. Small differences in the amount of ejecta with $Y_e \sim 0.1$ can have a factor $\sim$10 imprint in the abundance of actinides, with the potential to use these species as a diagnostic of the electron fraction of the disk outflow.

(5) The kilonova signature is quite similar in all models after the ejecta become optically thin, despite the aforementioned differences in the heating rate. More pronounced differences are found at early times when the ejecta are optically thick, with ALCAR models being brighter due in part to a more extended high-velocity tail given the more prominent neutrino-driven wind. We also find evidence of undersampling of the early ejecta with $\sim$2000 total particles, showing a significant brightening in FLASH models when 10 times more particles are used.

The expected boost in expansion velocity when including a large number of isotopes ($\sim$0.1 c relative to pure alpha

particles, Fig. 3) is consistent with what has been found in studies looking at the impact of *r*-process heating on the late-time evolution of disk outflows (e.g., [75]). Development of EOSs with more complete nuclear heating rates that also cover the relevant thermodynamic range for postmerger evolution would be of high usefulness to postmerger modeling.

Further code comparison studies are needed to bracket uncertainties in theoretical predictions for kilonova light curves and *r*-process nucleosynthesis yields, as more events with electromagnetic counterparts are anticipated in the future. While a first code comparison of GRMHD models has been carried out recently covering short evolutionary timescales of tens of milliseconds [76], more extensive comparisons of GRMHD models include a microphysical EOS and neutrino transport are needed. The high computational costs of these calculations makes extensive comparisons impractical at present, however, but nevertheless highly desirable for the future.

ACKNOWLEDGMENTS

R. F. acknowledges support from the Natural Sciences and Engineering Research Council of Canada (NSERC) through Discovery Grants No. RGPIN-2017-04286 and No. RGPIN-2022-03463. A sabbatical visit, during which this work was conceived and partially completed, was supported by the Cluster Project ELEMENTS from the State of Hesse and the European Research Council (ERC) under the European Union's Horizon 2020 research and innovation programme (ERC Advanced Grant KILONOVA No. 885281). R. F. is also grateful for the hospitality of the GSI Helmholtz Centre for Heavy Ion Research and the Institute of Physics, Academia Sinica, where part of this work was also conducted. O. J. acknowledges support by the ERC under the European Union's Horizon 2020 research and innovation programme under Grant Agreement No. 759253. G. M. P. and Z. X. acknowledge support by the ERC under the European Union's Horizon 2020 research and innovation programme (ERC Advanced Grant KILONOVA No. 885281). O. J., G. M. P., and Z. X. also acknowledge support by Deutsche Forschungsgemeinschaft (DFG, German Research Foundation)—Projects ID No. 279384907—SFB 1245 and No. MA 4248/3–1, and the State of Hesse within the Cluster Project ELEMENTS. Some of the software used in this work was in part developed by U.S. Department of Energy (DOE) NNSA-ASC OASCR Flash Center at the University of Chicago. We also acknowledge support from the Shared Hierarchical Academic Research Computing Network (SHARCNET) and the Digital Research Alliance of Canada (www.alliancecan.ca). FLASH models were run on the *Niagara* supercomputer at the SciNet HPC Consortium [77,78] and analyzed on the *graham* cluster at the University of Waterloo. SciNet is funded by the Canada Foundation for Innovation, the Government of Ontario (Ontario Research Fund—Research Excellence), and by the University of Toronto. R. F. also acknowledges storage resources of the National Energy Research Scientific Computing Center (NERSC), a DOE Office of Science User Facility using NERSC Award No. NP-ERCAP0024213. We are also grateful for computational support by the VIRGO cluster at GSI and the HOKUSAI computer center at RIKEN.

APPENDIX: NUCLEAR STATISTICAL EQUILIBRIUM FOR IONS

Here we provide the explicit relations defining nuclear statistical equilibrium for the ion component of the equation of state. Chemical equilibrium leads to the stoichiometric equations for the chemical potentials associated with reactions relating particle species, combined with mass and charge conservation. For a gas of neutrons, protons, alpha particles, and ^{54}Mn nuclei, we have

$$2\mu_{\rm n} + 2\mu_{\rm p} = \mu_\alpha, \tag{A1}$$

$$12\mu_\alpha + 5\mu_{\rm n} + \mu_{\rm p} = \mu_{\rm Mn}, \tag{A2}$$

$$X_{\rm n} + X_{\rm p} + X_\alpha + X_{\rm Mn} = 1, \tag{A3}$$

$$X_{\rm p} + \frac{1}{2}X_\alpha + \frac{25}{54}X_{\rm Mn} = Y_e, \tag{A4}$$

where the subscripts $\{{\rm n}, {\rm p}, \alpha, {\rm Mn}\}$ correspond to neutrons, protons, alpha particles, and ^{54}Mn nuclei, μ_i are the chemical potentials, X_i are the mass fractions, and Y_e is the electron fraction. If particles follow a Maxwell-Boltzmann distribution, we have

$$\mu_i = k_{\rm B}T\left[\ln\left(\frac{n_i}{n_{\rm Q,i}}\right) - \ln\omega_i\right] - \chi_i, \tag{A5}$$

where χ_i is the nuclear binding energy, ω_i is the nuclear partition function, n_i is the number density, and

$$n_{\rm Q,i} = \left(\frac{m_i k_{\rm B} T}{2\pi\hbar^2}\right)^{3/2} \tag{A6}$$

is the quantum concentration of particle species i. The stoichiometric equations for the chemical potential then become Saha equations for each dissociation/recombination channel.

Solution of the system of Eqs. (A1)–(A4) yields the equilibrium mass fractions for each species, as a function of density, temperature, and electron fraction $X_i^{\rm NSE}(\rho, T, Y_e)$. The nuclear binding energy contribution to the specific internal energy is included as

$$e_{\rm int} = e^0_{\rm int} - \frac{\chi_\alpha}{m_\alpha}X_\alpha - \frac{\chi_{\rm Mn}}{m_{\rm Mn}}X_{\rm Mn}, \tag{A7}$$

where $e^0_{\rm int}$ is the internal energy excluding nuclear binding energy, and m_i is the mass of particle species i. For a nonrelativistic ion gas, we have

$$e^0_{\rm int} = \frac{3}{2}\frac{k_{\rm B}T}{m_n}\sum_i \frac{X_i}{A_i}. \tag{A8}$$

For an equation of state in which the temperature is found from the internal energy using a Newton-Raphson scheme (as in FLASH), the derivatives of the mass fractions in NSE with respect to temperature must also be calculated to obtain the total temperature derivative of the internal energy as defined in Eq. (A7).

The original FLASH implementation does not account for ^{54}Mn nuclei, thus Eq. (A2) is not included, and $X_{\rm Mn} = 0$ everywhere else [including in Eq. (A7)]. NSE is solved for by solving the Saha equation for α particles directly. To include ^{54}Mn nuclei in the extended set of simulations, we generate a table of {n, p, α, Mn} mass fractions and associated temperature derivatives $(\partial X_i^{\rm NSE}/\partial T)_{\rho,Y_e}$ using the code[3] of [72] and constant partition functions $\omega_{\rm n} = \omega_{\rm p} = 2$ and $\omega_\alpha = \omega_{\rm Mn} = 1$. The table covers the range $T \in [5, 100] \times 10^9$ K, $\log_{10}\rho \in [1, 12]$, and $Y_e \in [0.01, 0.99]$. The ion internal energy is then computed using Eqs. (A7) and (A8).

[3]Available at https://cococubed.com/.

[1] B. P. Abbott *et al.*, Multi-messenger observations of a binary neutron star merger, Astrophys. J. **848**, L12 (2017).
[2] M. R. Drout *et al.*, Light curves of the neutron star merger GW170817/SSS17a: Implications for r-process nucleosynthesis, Science **358**, 1570 (2017).
[3] R. Fernández and B. D. Metzger, Electromagnetic signatures of neutron star mergers in the Advanced LIGO era, Annu. Rev. Nucl. Part. Sci. **66**, 23 (2016).
[4] L. Baiotti and L. Rezzolla, Binary neutron star mergers: A review of Einstein's richest laboratory, Rep. Prog. Phys. **80**, 096901 (2017).
[5] D. Radice, S. Bernuzzi, and A. Perego, The dynamics of binary neutron star mergers and GW170817, Annu. Rev. Nucl. Part. Sci. **70**, 95 (2020).
[6] H. T. Janka and A. Bauswein, Dynamics and equation of state dependencies of relevance for nucleosynthesis in supernovae and neutron star mergers, in *Handbook of Nuclear Physics* (Springer, Singapore, 2022), 10.1007/978-981-19-6345-2_93.
[7] D. M. Siegel and B. D. Metzger, Three-dimensional GRMHD simulations of neutrino-cooled accretion disks from neutron star mergers, Astrophys. J. **858**, 52 (2018).
[8] O. Just, S. Goriely, H. T. Janka, S. Nagataki, and A. Bauswein, Neutrino absorption and other physics dependencies in neutrino-cooled black hole accretion discs, Mon. Not. R. Astron. Soc. **509**, 1377 (2022).
[9] R. Popham, S. E. Woosley, and C. Fryer, Hyperaccreting black holes and gamma-ray bursts, Astrophys. J. **518**, 356 (1999).
[10] T. Di Matteo, R. Perna, and R. Narayan, Neutrino trapping and accretion models for gamma-ray bursts, Astrophys. J. **579**, 706 (2002).
[11] S. Setiawan, M. Ruffert, and H.-T. Janka, Non-stationary hyperaccretion of stellar-mass black holes in three dimensions: torus evolution and neutrino emission, Mon. Not. R. Astron. Soc. **352**, 753 (2004).
[12] W.-X. Chen and A. M. Beloborodov, Neutrino-cooled accretion disks around spinning black holes, Astrophys. J. **657**, 383 (2007).
[13] S. De and D. M. Siegel, Igniting weak interactions in neutron star postmerger accretion disks, Astrophys. J. **921**, 94 (2021).
[14] B. D. Metzger, A. L. Piro, and E. Quataert, Neutron-rich freeze-out in viscously spreading accretion discs formed from compact object mergers, Mon. Not. R. Astron. Soc. **396**, 304 (2009).
[15] B. D. Metzger and R. Fernández, Red or blue? A potential kilonova imprint of the delay until black hole formation following a neutron star merger, Mon. Not. R. Astron. Soc. **441**, 3444 (2014).
[16] O. Just, A. Bauswein, R. A. Pulpillo, S. Goriely, and H.-T. Janka, Comprehensive nucleosynthesis analysis for ejecta of compact binary mergers, Mon. Not. R. Astron. Soc. **448**, 541 (2015).
[17] S. Fujibayashi, K. Kiuchi, N. Nishimura, Y. Sekiguchi, and M. Shibata, Mass ejection from the remnant of a binary neutron star merger: Viscous-radiation hydrodynamics study, Astrophys. J. **860**, 64 (2018).
[18] S. Fujibayashi, S. Wanajo, K. Kiuchi, K. Kyutoku, Y. Sekiguchi, and M. Shibata, Postmerger mass ejection of low-mass binary neutron stars, Astrophys. J. **901**, 122 (2020).
[19] I. M. Christie, A. Lalakos, A. Tchekhovskoy, R. Fernández, F. Foucart, E. Quataert, and D. Kasen, The role of magnetic field geometry in the evolution of neutron star merger accretion discs, Mon. Not. R. Astron. Soc. **490**, 4811 (2019).
[20] K. Hayashi, S. Fujibayashi, K. Kiuchi, K. Kyutoku, Y. Sekiguchi, and M. Shibata, General-relativistic neutrino-radiation magnetohydrodynamic simulation of seconds-long black hole-neutron star mergers, Phys. Rev. D **106**, 023008 (2022).

[21] K. Hayashi, K. Kiuchi, K. Kyutoku, Y. Sekiguchi, and M. Shibata, General-relativistic neutrino-radiation magnetohydrodynamics simulation of seconds-long black hole-neutron star mergers: Dependence on initial magnetic field strength, configuration, and neutron-star equation of state, Phys. Rev. D **107**, 123001 (2023).
[22] R. Fernández and B. D. Metzger, Delayed outflows from black hole accretion tori following neutron star binary coalescence, Mon. Not. R. Astron. Soc. **435**, 502 (2013).
[23] R. Fernández, D. Kasen, B. D. Metzger, and E. Quataert, Outflows from accretion discs formed in neutron star mergers: Effect of black hole spin, Mon. Not. R. Astron. Soc. **446**, 750 (2015).
[24] R. Fernández, E. Quataert, J. Schwab, D. Kasen, and S. Rosswog, The interplay of disc wind and dynamical ejecta in the aftermath of neutron star-black hole mergers, Mon. Not. R. Astron. Soc. **449**, 390 (2015).
[25] R. Fernández, F. Foucart, D. Kasen, J. Lippuner, D. Desai, and L. F. Roberts, Dynamics, nucleosynthesis, and kilonova signature of black hole–neutron star merger ejecta, Classical Quantum Gravity **34**, 154001 (2017).
[26] S. Fahlman and R. Fernández, Hypermassive neutron star disk outflows and blue kilonovae, Astrophys. J. **869**, L3 (2018).
[27] S. Fujibayashi, M. Shibata, S. Wanajo, K. Kiuchi, K. Kyutoku, and Y. Sekiguchi, Mass ejection from disks surrounding a low-mass black hole: Viscous neutrino-radiation hydrodynamics simulation in full general relativity, Phys. Rev. D **101**, 083029 (2020).
[28] R. Fernández, F. Foucart, and J. Lippuner, The landscape of disc outflows from black hole-neutron star mergers, Mon. Not. R. Astron. Soc. **497**, 3221 (2020).
[29] B. D. Metzger and R. Fernández, From neutrino- to photon-cooled in three years: Can fallback accretion explain the X-ray excess in GW170817?, Astrophys. J. **916**, L3 (2021).
[30] O. Just, S. Abbar, M.-R. Wu, I. Tamborra, H.-T. Janka, and F. Capozzi, Fast neutrino conversion in hydrodynamic simulations of neutrino-cooled accretion disks, Phys. Rev. D **105**, 083024 (2022).
[31] S. Fujibayashi, K. Kiuchi, S. Wanajo, K. Kyutoku, Y. Sekiguchi, and M. Shibata, Comprehensive study of mass ejection and nucleosynthesis in binary neutron star mergers leaving short-lived massive neutron stars, Astrophys. J. **942**, 39 (2023).
[32] R. Fernández, S. Richers, N. Mulyk, and S. Fahlman, Fast flavor instability in hypermassive neutron star disk outflows, Phys. Rev. D **106**, 103003 (2022).
[33] M. Haddadi, M. D. Duez, F. Foucart, T. Ramirez, R. Fernandez, A. L. Knight, J. Jesse, F. Hebert, L. E. Kidder, H. P. Pfeiffer, and M. A. Scheel, Late-time post-merger modeling of a compact binary: Effects of relativity, r-process heating, and treatment of transport effects, Classical Quantum Gravity **40**, 085008 (2023).
[34] R. Fernández, A. Tchekhovskoy, E. Quataert, F. Foucart, and D. Kasen, Long-term GRMHD simulations of neutron star merger accretion discs: Implications for electromagnetic counterparts, Mon. Not. R. Astron. Soc. **482**, 3373 (2019).
[35] O. E. B. Messer, A. Mezzacappa, S. W. Bruenn, and M. W. Guidry, A comparison of Boltzmann and multigroup flux-limited diffusion neutrino transport during the postbounce shock reheating phase in core-collapse supernovae, Astrophys. J. **507**, 353 (1998).
[36] S. Yamada, H.-T. Janka, and H. Suzuki, Neutrino transport in type II supernovae: Boltzmann solver vs. Monte Carlo method, Astron. Astrophys. **344**, 533 (1999).
[37] M. Liebendörfer, M. Rampp, H. T. Janka, and A. Mezzacappa, Supernova simulations with Boltzmann neutrino transport: A comparison of methods, Astrophys. J. **620**, 840 (2005).
[38] S. Richers, H. Nagakura, C. D. Ott, J. Dolence, K. Sumiyoshi, and S. Yamada, A detailed comparison of multidimensional Boltzmann neutrino transport methods in core-collapse supernovae, Astrophys. J. **847**, 133 (2017).
[39] O. Just, R. Bollig, H. T. Janka, M. Obergaulinger, R. Glas, and S. Nagataki, Core-collapse supernova simulations in one and two dimensions: Comparison of codes and approximations, Mon. Not. R. Astron. Soc. **481**, 4786 (2018).
[40] E. O'Connor, R. Bollig, A. Burrows, S. Couch, T. Fischer, H.-T. Janka, K. Kotake, E. J. Lentz, M. Liebendörfer, O. E. B. Messer, A. Mezzacappa, T. Takiwaki, and D. Vartanyan, Global comparison of core-collapse supernova simulations in spherical symmetry, J. Phys. G **45**, 104001 (2018).
[41] R. M. Cabezón, K.-C. Pan, M. Liebendörfer, T. Kuroda, K. Ebinger, O. Heinimann, A. Perego, and F.-K. Thielemann, Core-collapse supernovae in the hall of mirrors. A three-dimensional code-comparison project, Astron. Astrophys. **619**, A118 (2018).
[42] V. Varma, B. Müller, and M. Obergaulinger, A comparison of 2D Magnetohydrodynamic supernova simulations with the COCONUT-FMT and AENUS-ALCAR codes, Mon. Not. R. Astron. Soc. **508**, 6033 (2021).
[43] O. Just, M. Obergaulinger, and H.-T. Janka, A new multidimensional, energy-dependent two-moment transport code for neutrino-hydrodynamics, Mon. Not. R. Astron. Soc. **453**, 3386 (2015).
[44] M. Obergaulinger, Astrophysical magnetohydrodynamics and radiative transfer, Dissertation, Technische Universität München, München, 2008.
[45] A. Mignone, High-order conservative reconstruction schemes for finite volume methods in cylindrical and spherical coordinates, J. Comput. Phys. **270**, 784 (2014).
[46] I. V. Artemova, G. Bjoernsson, and I. D. Novikov, Modified Newtonian potentials for the description of relativistic effects in accretion disks around black holes, Astrophys. J. **461**, 565 (1996).
[47] H. T. Janka and E. Mueller, Neutrino heating, convection, and the mechanism of Type-II supernova explosions, Astron. Astrophys. **306**, 167 (1996).
[48] G. N. Minerbo, Maximum entropy Eddington factors., J. Quant. Spectrosc. Radiat. Transfer **20**, 541 (1978).
[49] S. W. Bruenn, Stellar core collapse—Numerical model and infall epoch, Astrophys. J. Suppl. Ser. **58**, 771 (1985).
[50] C. J. Horowitz, Weak magnetism for antineutrinos in supernovae, Phys. Rev. D **65**, 043001 (2002).
[51] J. A. Pons, J. A. Miralles, and J. M. A. Ibanez, Legendre expansion of the $\nu\bar{\nu}$-annihilation, Astron. Astrophys. Suppl. Ser. **129**, 343 (1998).
[52] S. Hannestad and G. Raffelt, Supernova neutrino opacity from nucleon-nucleon bremsstrahlung and related processes, Astrophys. J. **507**, 339 (1998).

[53] E. O'Connor, An open-source neutrino radiation hydrodynamics code for core-collapse supernovae, Astrophys. J. Suppl. Ser. **219**, 24 (2015).
[54] O. Just, M. Obergaulinger, H.-T. Janka, A. Bauswein, and N. Schwarz, Neutron-star merger ejecta as obstacles to neutrino-powered jets of gamma-ray bursts, Astrophys. J. **816**, L30 (2016).
[55] B. Fryxell, K. Olson, P. Ricker, F. X. Timmes, M. Zingale, D. Q. Lamb, P. MacNeice, R. Rosner, J. W. Truran, and H. Tufo, FLASH: An adaptive mesh hydrodynamics code for modeling astrophysical thermonuclear flashes, Astrophys. J. Suppl. Ser. **131**, 273 (2000).
[56] A. Dubey, K. Antypas, M. K. Ganapathy, L. B. Reid, K. Riley, D. Sheeler, A. Siegel, and K. Weide, Extensible component-based architecture for flash, a massively parallel, multiphysics simulation code, J. Parallel Comput. **35**, 512 (2009).
[57] P. Colella and P. R. Woodward, The Piecewise Parabolic Method (PPM) for gas-dynamical simulations, J. Comput. Phys. **54**, 174 (1984).
[58] R. Fernández, Hydrodynamics of core-collapse supernovae at the transition to explosion. I. Spherical symmetry, Astrophys. J. **749**, 142 (2012).
[59] R. Fernández and B. D. Metzger, Nuclear dominated accretion flows in two dimensions. I. Torus evolution with parametric microphysics, Astrophys. J. **763**, 108 (2013).
[60] J. Lippuner, R. Fernández, L. F. Roberts, F. Foucart, D. Kasen, B. D. Metzger, and C. D. Ott, Signatures of hypermassive neutron star lifetimes on r-process nucleosynthesis in the disc ejecta from neutron star mergers, Mon. Not. R. Astron. Soc. **472**, 904 (2017).
[61] M. Ruffert, H.-T. Janka, and G. Schaefer, Coalescing neutron stars—a step towards physical models. I. Hydrodynamic evolution and gravitational-wave emission, Astron. Astrophys. **311**, 532 (1996).
[62] F. X. Timmes and F. D. Swesty, The accuracy, consistency, and speed of an electron-positron equation of state based on table interpolation of the helmholtz free energy, Astrophys. J. Suppl. Ser. **126**, 501 (2000).
[63] J. J. Mendoza-Temis, M.-R. Wu, K. Langanke, G. Martínez-Pinedo, A. Bauswein, and H.-T. Janka, Nuclear robustness of the *r* process in neutron-star mergers, Phys. Rev. C **92**, 055805 (2015).
[64] O. Just, I. Kullmann, S. Goriely, A. Bauswein, H.-T. Janka, and C. E. Collins, Dynamical ejecta of neutron star mergers with nucleonic weak processes—II: Kilonova emission, Mon. Not. R. Astron. Soc. **510**, 2820 (2022).
[65] J. Barnes, D. Kasen, M.-R. Wu, and G. Martínez-Pinedo, Radioactivity and thermalization in the ejecta of compact object mergers and their impact on kilonova light curves, Astrophys. J. **829**, 110 (2016).
[66] M.-R. Wu, J. Barnes, G. Martínez-Pinedo, and B. D. Metzger, Fingerprints of heavy-element nucleosynthesis in the late-time lightcurves of kilonovae, Phys. Rev. Lett. **122**, 062701 (2019).
[67] E. R. Most, L. J. Papenfort, S. D. Tootle, and L. Rezzolla, On accretion discs formed in MHD simulations of black hole-neutron star mergers with accurate microphysics, Mon. Not. R. Astron. Soc. **506**, 3511 (2021).
[68] O. Just, V. Vijayan, Z. Xiong, A. Bauswein, S. Goriely, J. Guilet, H.-T. Janka, and G. Martínez-Pinedo, End-to-end kilonova models of neutron-star mergers with delayed black-hole formation, Astrophys. J. Lett. **951**, L12 (2023).
[69] N. I. Shakura and R. A. Sunyaev, Black holes in binary systems. Observational appearance, Astron. Astrophys. **24**, 337 (1973).
[70] J. M. Stone, J. E. Pringle, and M. C. Begelman, Hydrodynamical non-radiative accretion flows in two dimensions, Mon. Not. R. Astron. Soc. **310**, 1002 (1999).
[71] W. H. Lee, E. Ramirez-Ruiz, and D. López-Cámara, Phase transitions and he-synthesis-driven winds in neutrino cooled accretion disks: Prospects for late flares in short gamma-ray bursts, Astrophys. J. **699**, L93 (2009).
[72] I. R. Seitenzahl, F. X. Timmes, A. Marin-Laflèche, E. Brown, G. Magkotsios, and J. Truran, Proton-rich nuclear statistical equilibrium, Astrophys. J. **685**, L129 (2008).
[73] S. Goriely, Uncertainties in the solar system r-abundance distribution, Astron. Astrophys. **342**, 881 (1999).
[74] I. U. Roederer, J. E. Lawler, E. A. Den Hartog, V. M. Placco, R. Surman, T. C. Beers, R. Ezzeddine, A. Frebel, T. T. Hansen, K. Hattori, E. M. Holmbeck, and C. M. Sakari, The R-process Alliance: A nearly complete R-process abundance template derived from ultraviolet spectroscopy of the R-process-enhanced Metal-poor Star HD 222925, Astrophys. J. Suppl. Ser. **260**, 27 (2022).
[75] H. Klion, A. Tchekhovskoy, D. Kasen, A. Kathirgamaraju, E. Quataert, and R. Fernández, The impact of r-process heating on the dynamics of neutron star merger accretion disc winds and their electromagnetic radiation, Mon. Not. R. Astron. Soc. **510**, 2968 (2022).
[76] P. L. Espino, G. Bozzola, and V. Paschalidis, Quantifying uncertainties in general relativistic magnetohydrodynamic codes, Phys. Rev. D **107**, 104059 (2023).
[77] C. Loken, D. Gruner, L. Groer, R. Peltier, N. Bunn, M. Craig, T. Henriques, J. Dempsey, C.-H. Yu, J. Chen, L. J. Dursi, J. Chong, S. Northrup, J. Pinto, N. Knecht, and R. Van Zon, SciNet: Lessons learned from building a power-efficient Top-20 system and data centre, in J. Phys. Conf. Ser. **256**, 012026 (2010).
[78] M. Ponce, R. van Zon, S. Northrup, D. Gruner, J. Chen, F. Ertinaz, A. Fedoseev, L. Groer, F. Mao, B. C. Mundim, M. Nolta, J. Pinto, M. Saldarriaga, V. Slavnic, E. Spence, C.-H. Yu, and W. R. Peltier, Deploying a top-100 supercomputer for large parallel workloads: The Niagara supercomputer, PEARC '19: Proceedings of the Practice and Experience in Advanced Research Computing on Rise of the Machines (Learning) (2019), 10.1145/3332186.3332195.